

HIGH-SPEED SERIAL-KINEMATIC SPM SCANNER: DESIGN AND DRIVE CONSIDERATIONS

Kam K. Leang and Andrew J. Fleming

ABSTRACT

This paper describes the design of a flexure-guided, two-axis nanopositioner (scanner) driven by piezoelectric stack actuators. The scanner is specifically designed for high-speed scanning probe microscopy (SPM) applications, such as atomic force microscopy (AFM). A high-speed AFM scanner is an essential component for acquiring high-resolution, three-dimensional, time-lapse images of fast processes such as the rapid movement of cells and the diffusion of DNA molecules. A two-axis SPM scanner is proposed, where the slow and fast scanning axes are serially connected and flexure guided to minimize runout. The scanner's achievable scan range is approximately $10\ \mu\text{m} \times 10\ \mu\text{m}$. Finite element analysis is utilized to optimize the mechanical resonance frequencies of the scanner. Experimental results show a first major resonance in the slow and fast axis at 1.5 and 29 kHz, respectively. This paper also discusses the various tradeoffs between speed, range, electrical requirements, and scan trajectory design for high-speed nanopositioning.

Key Words: High-speed nanopositioning, piezoactuator, scanning probe microscope.

I. INTRODUCTION

The dynamic behavior of biological cells, DNA, and molecules occur at time scales much faster than the measurement capabilities of conventional scanning probe microscopes (SPMs), for example an atomic force microscope (AFM). AFMs capable of high-speed operation are required to observe these processes in real-time [1]. Also, high-speed positioning is desirable for high-throughput, probe-based nanomanufacturing. Primarily a serial technique, the total process time of probe-based fabrication is proportional to the number of desired features [2]. Therefore, a high-throughput positioning stage can drastically reduce manufacturing time. A serial-kinematic nanopositioning stage (scanner) is proposed for high-speed nanopositioning and SPM-based applications.

The earlier work by Ando and co-workers [3] focused on exploiting stiff piezo-stack actuators to create a scanner with high resonance frequency. The researchers demonstrated imaging at 12.5 frames/s (100×100 pixels per image), and they used the system to capture

Manuscript received March 10, 2008; accepted August 8, 2008.

Kam K. Leang is with the Department of Mechanical Engineering, University of Nevada, Reno, NV, 89557-0312, USA (e-mail: kam@unr.edu).

Andrew J. Fleming is with the School of Electrical Engineering and Computer Science, The University of Newcastle, Callaghan, NSW 2308, Australia (e-mail: Andrew.Fleming@newcastle.edu.au).

This research was supported, in part, by the National Science Foundation, Grants DUE #0633098 and CMMI #0726778, the Australian Research Council (DP0666620) and the ARC Centre of Excellence for Complex Dynamic Systems and Control. Experiments were performed at the Laboratory for Dynamics and Control of Nanosystems, University of Newcastle. The authors would like to thank Ken Sayce from the University of Newcastle, David Modlin from 3D Enterprises, and Matthew Vaerewyck and Joseph Garthaffner from Virginia Commonwealth University, Richmond, VA, for their help in fabricating the scanner.

real-time video of biological specimens [4]. Schitter and co-workers also developed a scanner based on piezo-stack actuators, but in their design the actuators were arranged in a push-pull configuration and mechanical flexures were used to decouple the lateral and transverse motions [5]. In this case, the finite element analysis (FEA) method was used to optimize the performance of the mechanical structure [6]. The reported AFM imaging rate was 8 frames/s (256×256 pixels). By exploiting the stiffness of shear piezos and a compact design, a scanner was created for imaging up to 80 frames/s (128×128 pixels) with a line rate of 10.2 kHz [7]. The achievable range of motion was $300 \text{ nm} \times 300 \text{ nm}$. A unique approach for high-speed scanning involving a piezo-stack actuator combined with a tuning fork is reported in [8]. The tuning fork operated at resonance and AFM images were acquired at 100 frames/s (128×128 pixels). Likewise, a combined flexure-based scanner and tuning fork achieved imaging rate in excess of 1000 frames/s in [9].

This paper focuses on a serial-kinematic scanner design. The serial-kinematic configuration is suitable for SPM applications because motion along the lateral axis (x) is typically at least 100-times faster than the slower, transverse axis (y). For example, to acquire a 100×100 pixel-resolution image at the rate of one frame per second, the scanner moves laterally back and forth across a sample surface at 100 Hz while the motion along the transverse axis is 1 Hz. Therefore, the fast and slow axis can be designed independently. The requirement for only one high-speed axis reduces the design complexity and cost. Additionally, high-bandwidth control hardware is only required for one direction, where parallel-kinematic scanners employ two [5]. Although the serial configuration is simple to design and cost effective, a penalty is that high resonance frequency can only be achieved in one axis. This paper also considers the tradeoffs between speed, range, required control hardware, cost, and manufacturability.

In Section II, design objectives are discussed. Following that, details of the mechanical design are presented in Section III. Sections V and IV discuss the design of input trajectories and the electrical requirements of the driving amplifier, respectively. Experimental results are presented in Section VI to demonstrate the performance of a prototype scanner. Finally, the paper is concluded in Section VII.

II. DESIGN OBJECTIVES AND CONSIDERATIONS

The goal is to develop a high-speed scanner capable of moving a sample relative to an SPM probe

tip. First, the target frame rate is 30 frames per second, where each frame is 100×100 pixels. Second, the desired scan range is $\geq 10 \mu\text{m} \times 10 \mu\text{m}$. This range enables the AFM to observe a wide spectrum of specimens and samples, from micron-size cells to submicron-size subjects such as DNA. Finally, the system should be cost effective to manufacture.

The design process to optimizing the mechanical and electrical design of the scanner includes: (1) identifying relevant design tradeoffs, (2) optimizing the mechanical design of the scanner using FEA, (3) developing the necessary electronic hardware for the scanner, and (4) considering the use of input-shaping to enable high-speed scanning. Attention is focused on the motion parallel to the sample surface, *i.e.*, along the lateral (x) and transverse (y) directions. Motion along the vertical axis (z) is not considered.

The important design parameters are: (i) the first dominant resonant frequency, (ii) the scan range, (iii) the power supply requirements (voltage, current, and bandwidth), and (iv) cost and manufacturability. The first two design parameters, (i) and (ii), conflict directly with one another. Large range implies low stiffness and hence low first resonance frequencies [6]. The third design parameter restricts the amount of voltage, current, and power that can be supplied to the actuator. In turn, this restricts the type and dimensions of the piezoactuator that can be used for positioning. Larger piezoelectric actuators can provide greater stroke, but have higher capacitance and require more power at high frequencies. The final consideration is cost and manufacturability. The scanner fabrication should not utilize any exotic materials or processes and should be tolerant of typical machining tolerances.

III. THE MECHANICAL DESIGN

3.1 Serial versus parallel kinematic configuration

For scanning in two directions, there are two basic configurations: serial and parallel kinematics. In a serial kinematic system, for example the design used by several commercial vendors of scanning stages and in [4], there is exactly one actuator (and sensor) for each degree of freedom (see Fig. 1(a)). One disadvantage of this design is the inability to measure (and correct for) parasitic motion such as runout or guiding error. Although the serial configuration is simple to design, a penalty is that high resonance frequency can only be achieved in one axis.

In a parallel kinematic scanning stage, *e.g.*, Schitter *et al.*'s work [10], all actuators are connected

in parallel to the sample platform (see Fig. 1(b)). This arrangement enables rotation of the image, *i.e.*, the fast scanning axis can be chosen arbitrarily. An advantage of this configuration is that parasitic motion due to runout and guiding error can easily be measured and corrected. However, since the mechanical dynamics of both the lateral and transverse axes are similar, high-bandwidth control hardware is required for both directions. In contrast, for the serial-kinematic configuration only the high-speed axis requires high power and wide bandwidth performance, reducing overall cost.

The spring constants k_x and k_y in Fig. 1 for both the serial and parallel kinematic configurations may include the stiffness of added flexures in each direction. To achieve high resonance frequencies, the effective spring constants should be as stiff as possible while maintaining low effective mass. The effects of inertial force generated by the sample platform during scanning must also be taken into account. The flexures must provide enough preload to avoid exposing the stack actuator to damaging tensional forces.

While the resonance frequency of the fast axis is of primary concern, the slow-axis resonance frequency can essentially be ignored. For example, the scan rate of the slow axis is one-hundredth the scan rate of the fast-axis when acquiring a 100×100 pixel image. Therefore, the fast-scan axis can be designed independently without any significant consideration for performance implications on the slow-scan axis.

3.2 Piezoactuator considerations

The actuating mechanism of choice for scanning at high speed is the piezoactuator [11]. Different types of piezoactuators are compared in Table I. Piezo-stack actuators offer high stiffness, but limited range

of motion. The geometry of a stack compared to a tube-shaped piezoactuator results in higher resonance frequencies for the same deflection [12]. Thin shear-piezos offer high resonance frequency, but small range (sub-micron) [7].

To achieve the desired scan range of $10 \mu\text{m} \times 10 \mu\text{m}$, the Noliac SCMA-P7 piezoelectric stack actuators were chosen ($5 \text{ mm} \times 5 \text{ mm} \times 10 \text{ mm}$, 380 nF). Figure 2(b) shows a photograph of the piezo-stack actuator. The actuator's unloaded stroke is $11.8 \mu\text{m}$, with an unloaded resonance frequency of 220 kHz , stiffness of $283 \text{ N}/\mu\text{m}$, and blocking force of 1000 N . The elastic modulus calculated from the blocking pressure P_B and strain ε is $E = \frac{P_B}{\varepsilon} = 33.9 \text{ GPa}$. It is noted that although a greater cross-sectional area would increase stiffness, the proportional increase in capacitance would occur. This in turn would increase the required power, a highly undesirable consequence.

3.3 Preloading piezo-stack actuators

Piezo-stacks are intolerant to tensile (as well as shear) stresses. Because stacks are constructed of glued (or fused) piezoelectric layers, tensional loads can cause the actuators to fail at the interface (glue) layers. Manufacturers often specify a tensile load limit less than 10% of the compressive load limit. During high-speed operation, inertial forces due to the sample mass must be taken into account to avoid excessive tensile stresses. A preload force must be incorporated to eliminate the possibility of the actuator being exposed to excessive tensile forces. The preload must be applied in such a way that full surface contact is achieved to assure good load distribution.

Flexures can be used to apply the appropriate preload on the piezo-stack actuator. The flexures serve two purposes: to eliminate tensile stress and to guide

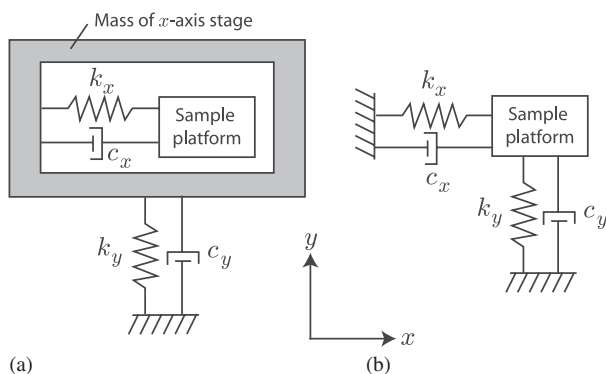


Fig. 1. Configurations for two-axis scanning: (a) serial and (b) parallel kinematics arrangement. The spring constants k_x and k_y include the stiffness of the piezoactuators and added flexures in each direction.

Table I. A comparison of different piezoactuator types.

Actuator type	Stiffness	Range	Capacitance	Voltage
Piezo-bimorph	low	high	med	low-med
Piezo-tube	med	med	low	high
Piezo-plate	high	low	low	high
Piezo-stack	high	low-med	med-high	low

Table II. The mechanical properties of various metals [13].

Metal	Elastic modulus (GPa)	Yield strength (MPa)	Density (kg/cm^3)	Poisson's Ratio
Aluminum alloy	72	97	2800	0.33
Stainless steel	200	207	8000	0.30
Titanium	107	240	4510	0.36

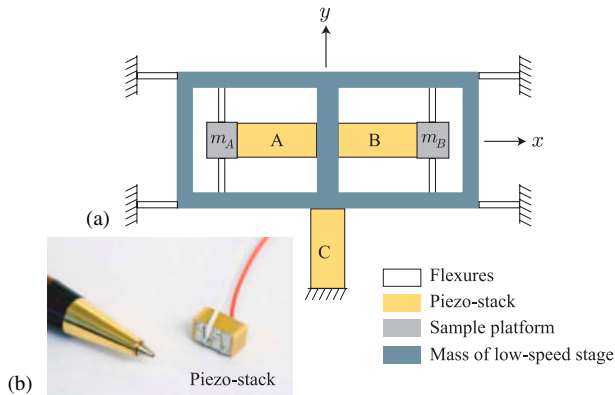


Fig. 2. (a) A sketch of the flexure-guided serial-kinematic scanner. Two opposing piezo-stack actuators, A and B, are used to compensate for the sample platform's inertial effects. The piezo-stack C moves the high-speed stage in the y direction. (b) A photograph of the piezo-stack actuator.

the extension/contraction of the actuator so that parasitic motion is minimized. The required preload was estimated from Newton's Second Law by computing the maximum sample platform acceleration during maximum excursion and scan frequency. In Section IV an input signal is designed that minimizes induced vibration. From the resulting scan motion, the minimum preload requirement is 20 N for a 2 g sample mass. With a safety factor of 2, the conservative preload specification is 40 N. The details of the flexure design is discussed next.

3.4 Optimizing the mechanical design using FEA

The finite element method (ANSYS, Canonsburg, PA, USA) is used to optimize the design of the scanner in both directions [6]. The first task is to design the high-speed x -axis scanning stage. Candidate materials for the stage assembly are listed in Table II [13]. Stainless steel and AISI A2 tool steel are listed for their high stiffness compared to the piezoelectric material. However, AISI A2 steel requires proper heat treating to achieve the equivalent elastic modulus as stainless steel. A standard heat-treating process is used, such as heating the material to 850°C, followed by cooling in the furnace at 10°C per hour to 650°C. Finally, the material is cooled freely in air. The other components that require a high stiffness to density ratio, such as the flexures and sample platform, are constructed from aluminum.

For the high-speed axis, the piezo-stack is fixed on one side, and the sample platform (plate) is attached to the free end. Preloading is achieved by using two flexures attached to the free end, connected to the sample platform, as shown in Fig. 2(a). Also shown in the figure is an opposing piezo-stack, which is added to

compensate for inertial force generated by the movement of the sample platform along the x -axis. The inertial force can induce undesirable dynamics on both the low- and high-speed stages.

The preload on the piezo-stack is achieved during stage assembly. In particular, by 'squeezing' the stack against the flexures using fasteners, preload is achieved. The dimensions of the flexures are designed to provide the appropriate preload when the stage is assembled. The flexures help to shift the first resonance frequency of the piezo-stack to a higher value compared to its cantilevered configuration. The flexure is designed using beam analysis and assuming linear-elastic material behavior. In the configuration shown in Fig. 2(a), the flexures are modeled as a fixed-fixed (clamp-clamp) beam with a point load P at the beam's midpoint. The maximum deflection δ_{max} for such a beam occurs at its midpoint [14], where the sample platform makes contact with the flexure,

$$\delta_{max} = \frac{PL^3}{192EI}. \quad (1)$$

In Eq. (1), E is the elastic modulus, L is the length (*i.e.*, combined length of both flexures), and $I = ht^3/12$ (t and h are the thickness and height of the flexure). Rewriting the deflection equation (1) as the ratio of the applied force to the maximum deflection, the flexure's spring constant becomes

$$K_f = \frac{192EI}{L^3}. \quad (2)$$

This expression is used to determine the required dimensions of the flexure given the stiffness K_f . For example, the stiffness of the flexure is designed to be approximately $1/20^{th}$ the stiffness of the piezo-stack, *i.e.*, $K_f = 10 \text{ N}/\mu\text{m}$. The low-speed stage is designed in a similar manner.

Due to manufacturing tolerances [± 0.001 in ($\pm 25 \mu\text{m}$)], the preload exerted by the flexure can be as high as 250 N. This value, though greater than the estimated value of 40 N, is acceptable. An assembly drawing and a photograph of the prototype two-axis high-speed scanner is shown in Fig. 3(a) and (b), respectively.

ANSYS FEA software is used to simulate the dynamics of the low- and high-speed stage. Material damping is ignored in the simulation because the objective is to predict the resonance frequencies. The small amount of damping in piezoelectric actuators and the

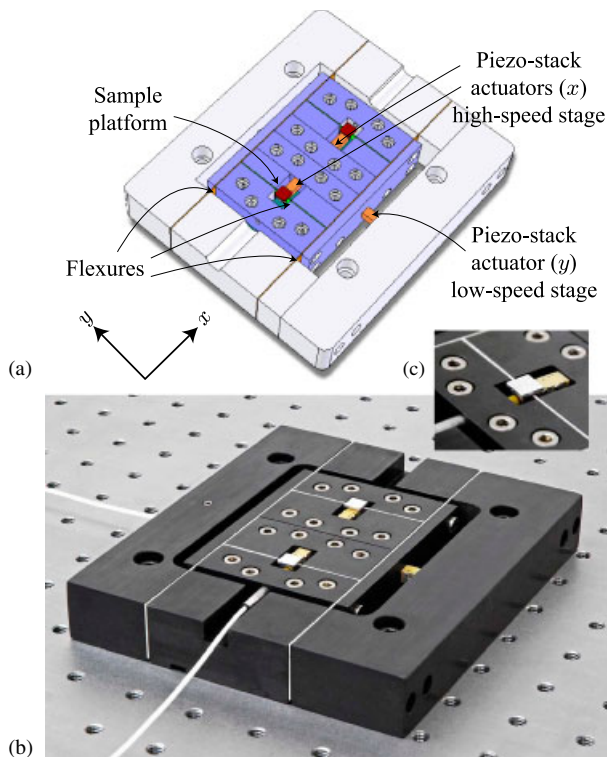


Fig. 3. (a) An assembly drawing of the two-axis high-speed scanner, where the high-speed stage (x) is nested inside of the low-speed stage (y). (b) A photograph of a manufactured scanner with black surface finish. (c) A close-up view of sample platform and x -axis piezo-stack actuator.

aluminum flexures would not have significant impact on the resonance frequencies. In fact, when damping is small, the resonance frequency is approximately the natural frequency. The simulated frequency response from applied voltage to the normalized displacement is plotted in Fig. 4. The three plots (top-to-bottom) show the magnitude responses of the x -, y - and z -axis, respectively. The edges of the flexures and the base of the piezo-stack are constrained in the FEA simulation; that is, body modes are neglected.

The simulation results in Fig. 4 indicate that the lowest resonance frequency occurs at approximately 28.5 kHz (the vertical cantilever mode of the piezo-stack). The next dominant mode is the side-to-side (y -axis) motion, which presents itself at 33 kHz. Finally, the piston mode of the piezo-stack (in the x -axis) occurs at 45 kHz. Along the low-speed axis, the dominant mode occurs at approximately 1.5 kHz. It is noted that the resonance frequency for the low-speed stage can be improved by reducing the mass of the high-speed stage. At low-frequency, approximately 600 Hz, a resonant zero appears in the cross-coupling transfer function as shown in Fig. 4, plots (a1) and (a3). The presence

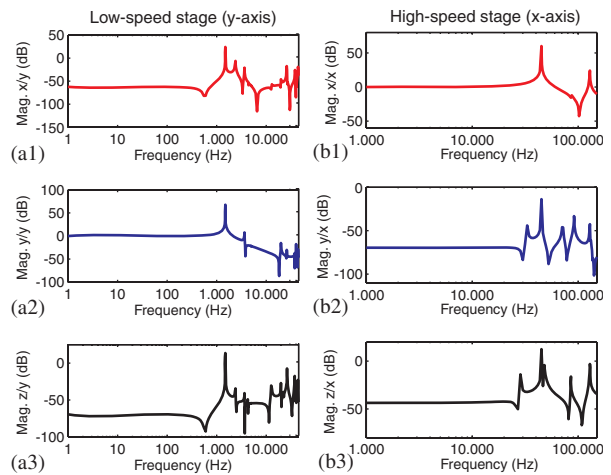


Fig. 4. Simulated frequency response for the low-speed (y -axis) stage, plots (a1) to (a3), and for the high-speed (x -axis) stage, plots (b1) to (b3).

of the zero does not affect the scanning as this is dictated by the y -to- y and x -to- x transfer functions shown in Fig. 4, plots (a2) and (b1), respectively.

IV. INPUT DESIGN

The characteristics of the input signal determines the maximum scan rate, induced vibration, minimum mechanical preload, and electrical requirements of the drive electronics. Therefore, the input signal significantly influences the overall scanner performance and should be optimized accordingly.

In high-speed applications, the primary goal is to achieve highest possible scan-rate from a given mechanical bandwidth. Various inversion-based feedforward controllers have been proposed with this aim, for example [15–18]. Unfortunately, such techniques require detailed plant models and are not intended to guarantee linear scanning (constant velocity) operation.

Recently, a technique was introduced to design periodic input signals with perfectly linear regions and optimal spectral characteristics [19]. The resulting signals minimize signal power above a certain frequency while guaranteeing linearity over a specified range. A key benefit is that only an estimate of the first resonance frequency is required during the design. The number of harmonics contained in the scanning signal and the range of linearity can be freely varied to achieve an arbitrarily low out-of-bandwidth power.

The technique is based on finding a signal y that is equal to a reference trajectory r at an arbitrary set of sample indexes S and free to vary elsewhere. The free

part of the signal is varied to minimize the quadratic cost $y^T H y$. That is, a solution y is found to satisfy

$$y = \arg \min_x x^T H x, \text{ subject to } x_k = r_k \text{ } k \in S, \quad (3)$$

where $x \in \mathfrak{R}^{N \times 1}$ and $H \in \mathfrak{R}^{N \times N}$. Equation (3) is equivalent to the linearly constrained convex quadratic optimization problem

$$y = \arg \min_x x^T H x + 2f^T x, \text{ subject to}$$

$$A x = r(S), \quad (4)$$

where A is the selection matrix representing S and $r(S)$ is a row vector containing the samples of r_n indexed by the values of S .

The signal (4) can be restated in matrix notation as

$$\begin{bmatrix} H & A^T \\ A & 0 \end{bmatrix} \begin{bmatrix} y \\ \lambda \end{bmatrix} = \begin{bmatrix} -f \\ r(S) \end{bmatrix}, \quad (5)$$

where λ are the Lagrange multipliers. Equation (5) has a solution

$$\begin{bmatrix} y \\ \lambda \end{bmatrix} = \begin{bmatrix} H & A^T \\ A & 0 \end{bmatrix}^{-1} \begin{bmatrix} -f \\ r(S) \end{bmatrix}. \quad (6)$$

It can be shown that minimum out-of-bandwidth power is achieved when [19]

$$H = \frac{1}{N^2} E^* W E, \quad (7)$$

where N is the number of samples per period, E is a fast Fourier transform matrix, and W is a weighting matrix defining which harmonics are penalized and which are to remain free. This technique is applied to determine an input for high-speed scanning.

With a first resonance frequency of 45 kHz (see Fig. 4), the scanner's useful bandwidth is 35 kHz where phase and amplitude deviation are negligible. With a scanning signal containing 7 harmonics (the 1st, 3rd, 5th and 7th), the maximum scan speed is 5 kHz. This corresponds to 25 frames/s at 200 × 200 resolution, or 50 frames/second at 100 × 100 resolution.

A 5 kHz scanning trajectory is designed using the tools described in reference [19].* The signal contains 7 significant harmonics and has a linear range of 60%, which equates to a maximum linear scan-range of 7 μm out of a possible 10 μm. The optimal input to achieve the 6 μm trajectory is plotted in Fig. 5(a) together with the industry standard minimum-acceleration signal. The minimum-acceleration signal has the same linear range

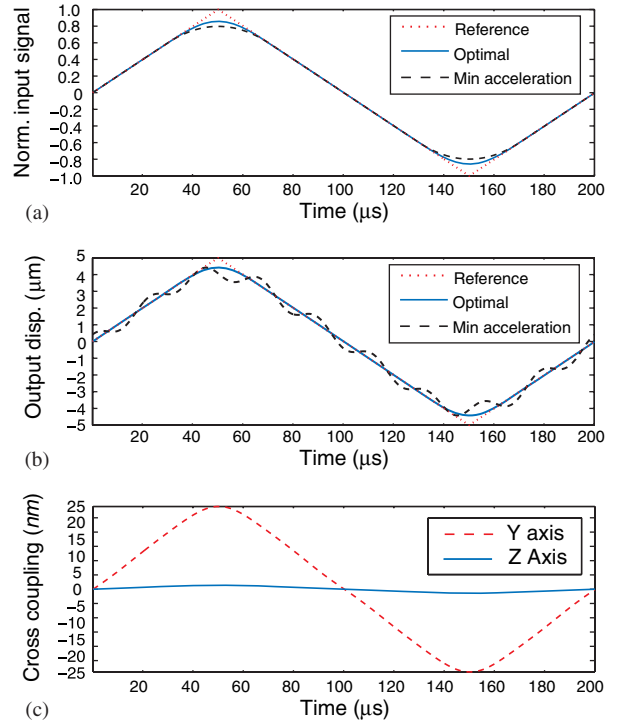


Fig. 5. (a) The scanner input signals: triangular, optimal, and minimum acceleration. (b) The simulated scanner displacement for the optimal and minimum acceleration input. (c) The y- and z-axis runout due to the x-axis trajectory shown in (b).

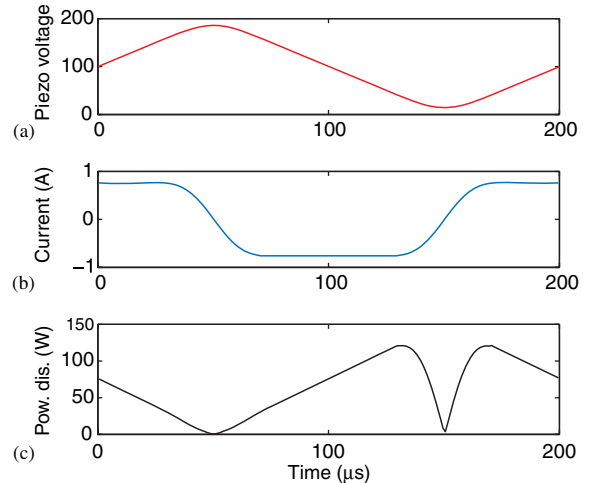


Fig. 6. The (a) voltage, (b) current, and (c) amplifier dissipation required to achieve the trajectory plotted in Fig. 5(b).

but follows a quadratic trajectory during the reverse in direction.

In the simulated x -axis displacement plotted in Fig. 5(b), the performance of the optimal signal is clearly demonstrated. The simulation model is obtained by fitting a state-space model to the data of Fig. 4 using

*Available from the second author.

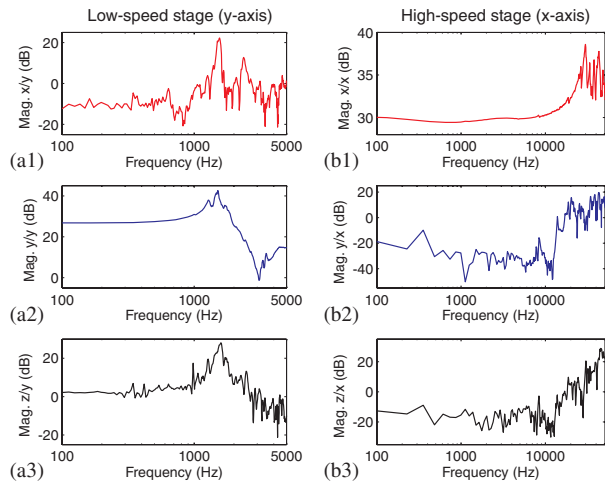


Fig. 7. Experimentally measured frequency response for the low-speed (y-axis) stage, plots (a1) to (a3), and for the high-speed (x-axis) stage, plots (b1) to (b3). Units are nm/V.

the frequency domain subspace algorithm. This technique provides excellent reduced order models over a certain bandwidth. The modal damping ratios are conservatively estimated at 0.005.

The force acting between the sample-mass and actuator can be computed from the numerical acceleration and sample mass using Newton's Second Law. For the trajectory plotted in Fig. 5(b), the maximum tensile force is 10 N per gram of sample. For a maximum load of 2 g and a safety factor of 2, the required preload force is 40 N.

A key scanner performance criteria that strongly influences image quality is the magnitude of runout in adjacent axes. In Fig. 5(c), the y- and z-axis runout resulting from the x-axis trajectory in Fig. 5(b) are plotted. The y-axis runout is less than 0.5% while the z-axis runout is approximately 0.03%. This magnitude of runout is capable of providing 200×200 resolution with negligible image overlap.

V. ELECTRICAL CONSIDERATIONS

Due to the capacitive nature of piezoelectric transducers, high speed operation requires large current and power dissipation. If the maximum driving voltage, trajectory, and frequency are known, the current and power dissipation are easily computed by conservatively approximating the transducer as a purely capacitive load. For example, the current $I_p = CsV_p$, where s is the Laplace variable, and C and V_p are the transducer capacitance (380 nF) and load voltage, respectively. The

power dissipation in a linear amplifier is $P_d = I_p(V_s - V_p)$, where V_s is the supply voltage (200 V). The current, voltage, and power dissipation corresponding to the input trajectory in Fig. 5(b) are plotted in Fig. 6. As the load is primarily reactive, the average power dissipation of 75 W is also the required supply power. These specifications can be achieved with standard amplifier configurations (Figure 7).

VI. EXPERIMENTAL RESULTS

The performance of the fabricated scanner is evaluated and compared to FEA results. The piezo-stack actuators are driven by a custom-made driver. A Polytec PSV300 scanning laser vibrometer is used to measure the x- and y-axis displacements as well as vibrational mode shapes.

The frequency response plots for the slow and fast scanning directions are shown in Fig. 7. In the y direction, the first major resonance (piston mode) occurs at approximately 1.5 kHz (see Fig. 7(a2)). This value agrees with the FEA simulation shown in Fig. 4(a2). In the x direction, the first major resonance occurred at approximately 29 kHz (see Fig. 7(b1)), which was under the estimated peak of 45 kHz.

Input voltage applied to the x axis can excite vertical modes of the piezo-stack. These modes are important as uncommanded vertical motion can cause large tip-to-sample forces, which can damage the cantilever or sample. The first four vertical modes are shown in Fig. 8, for resonances at 21, 28, 44, and 49 kHz. The first mode at 21 kHz behaved analogously to a clamped-clamped beam with nodes at either end of the piezo-stack. Thus, vertical motion of the sample platform at location A is insignificant (see Fig. 8(a)). The next mode at 28 kHz, Fig. 8(b), was a variation of the clamped-clamped mode with a small vertical motion at location A. In contrast, the modes at 44 and 49 kHz exhibit a node actuator midpoint and large deflections at location A (Figs 8(c) and (d)). Thus, the scanner bandwidth is limited by these vertical modes.

The time response of cross coupling effects are shown in Fig. 9. A 185 V peak-to-peak sine wave, applied to the y axis, induces an x axis displacement of 2.06% of the y axis range (7.42 μm , see Fig. 9(a1)). Likewise, motion in the z direction is 5.74% of the y range. A 185 V peak-to-peak sine wave, applied to the x axis (range 11.07 μm), induces 2.79% and 0.18% motion in the y and z direction, respectively.

A 100-Hz triangle input voltage (Fig. 10(c)) is applied to drive the high-speed stage. The measured

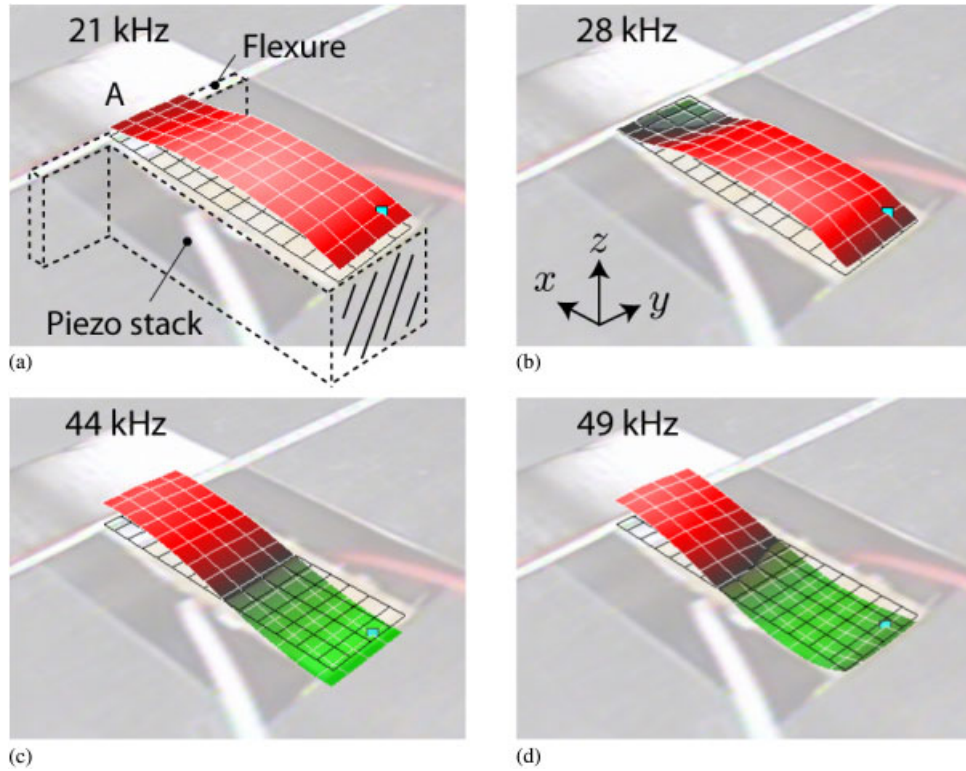


Fig. 8. Vertical modes of piezo-stack excited by input to x axis. Sample platform is located at A.

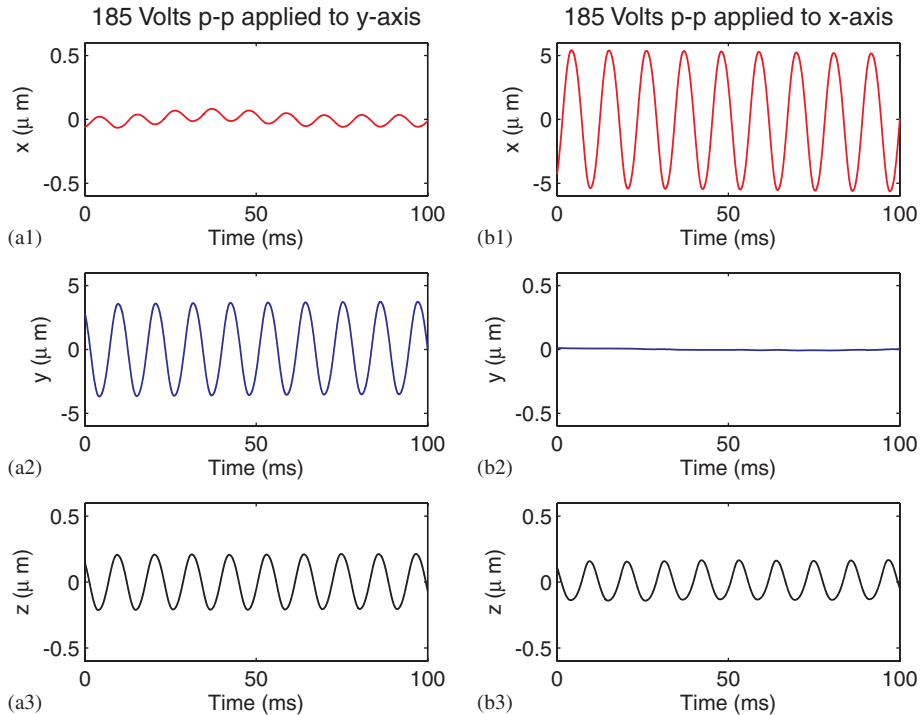


Fig. 9. Experimentally measured time response of cross-coupling for the low-speed (y -axis) stage, plots (a1) to (a3), and for the high-speed (x -axis) stage, plots (b1) to (b3). Input was a 185 V peak-to-peak sine wave at 100 Hz.

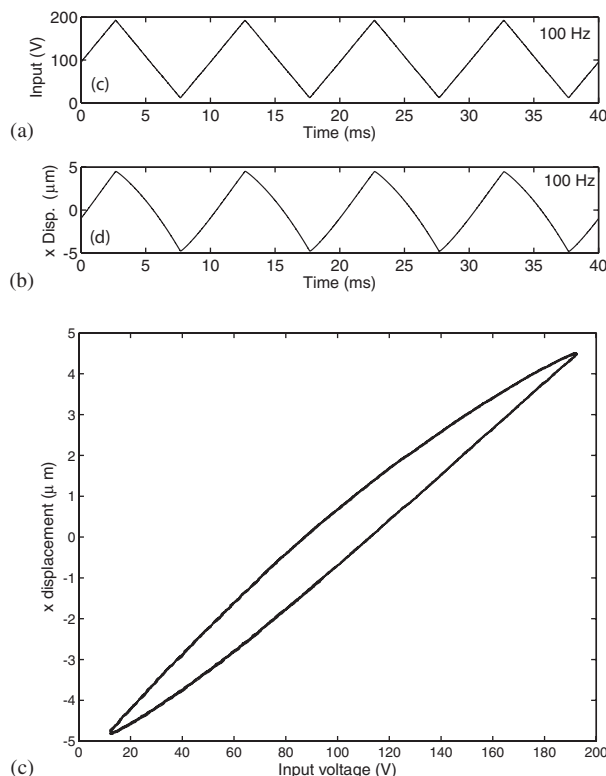


Fig. 10. High-speed stage's response to triangle input at 100 Hz: (a) input voltage versus time, (b) measured displacement versus time, and (c) hysteresis curve.

open-loop displacement is shown in Fig. 10(d). Over the range of $9.3 \mu\text{m}$, the maximum displacement hysteresis is approximately 15%. The hysteresis effect is significant in open-loop. Methods to compensate for the hysteresis, such as model-based feedforward approaches [15], high-gain feedback [20], and charge control [21] will improve the performance of the scanner.

VII. CONCLUSIONS

This paper described the design of a two-axis, serial-kinematic high-speed scanner based on piezo-stack actuators. The scanner's range is approximately $10 \mu\text{m} \times 10 \mu\text{m}$ and the fast scanning axis is optimized for speed. Experimental results showed a good correlation with simulation and a first resonance frequency of 29 kHz in the high-speed axis. This is sufficient to achieve SPM line rates of approximately 4 kHz.

REFERENCES

- Guthold, M., X. Zhu, and C. Rivetti *et al.* "Real-time imaging of one-dimensional diffusion and transcription by Escherichia coli RNA polymerase," *Biophys. J.*, Vol. 77, No. 4, pp. 2284–2294 (1999).
- Snow, E. S., P. M. Campbell, and F. K. Perkins, "Nanofabrication with proximal probes," *Proc. IEEE*, Vol. 85, No. 4, pp. 601–611 (1997).
- Ando, T., N. Kodera, D. Maruyama, E. Takai, K. Saito, and A. Toda, "A high-speed atomic force microscope for studying biological macromolecules in action," *Jpn. J. Appl. Phys. Part 1*, Vol. 41, No. 7B, pp. 4851–4856 (2002).
- Ando, T., N. Kodera, T. Uchihashi, A. Miyagi, R. Nakakita, H. Yamashita, and K. Matada, "High-speed atomic force microscopy for capturing dynamic behavior of protein molecules at work," *e-J. Surf. Sci. Nanotech.*, Vol. 3, pp. 384–392 (2005).
- Schitter, G., K. J. Astrom, B. E. DeMartini, P. J. Thurner, K. L. Turner, and P. K. Hansma, "Design and modeling of a high-speed AFM-scanner," *IEEE Trans. Control Syst. Technol.*, Vol. 15, No. 5, pp. 906–915 (2007).
- Kindt, J. H., G. E. Fantner, J. A. Cutroni, and P. K. Hansma, "Rigid design of fast scanning

- probe microscopes using finite element analysis,” *Ultramicroscopy*, Vol. 100, No. 3–4, pp. 259–265 (2004).
7. Rost, M.J., L. Crama, P. Schakel *et al.* “Scanning probe microscopes go video rate and beyond,” *Rev. Sci. Instrum.*, Vol. 76, pp. 053710-1–053710-9 (2005).
 8. Humphris, A. D. L., J. K. Hobbs, and M. J. Miles, “Ultrahigh-speed scanning near-field optical microscopy capable of over 100 frames per second,” *Appl. Phys. Lett.*, Vol. 83, No. 1, pp. 6–8 (2003).
 9. Picco, L. M., L. Bozec, A. Ulcinas, D. J. Engledew, M. Antognozzi, M. A. Horton, and M. J. Miles, “Breaking the speed limit with atomic force microscopy,” *Nanotechnology*, Vol. 18, pp. 044030 (2007).
 10. Schitter, G., “Advanced mechanical design and control methods for atomic force microscopy in real-time,” *Am. Control Conf.*, New York, USA, pp. 3503–3508 (2007).
 11. Moheimani, S. O. R. and A. J. Fleming, *Piezoelectric Transducers for Vibration Control and Damping (Advances in Industrial Control)*, Springer (2006).
 12. Binnig, G. and C. F. Quate, “Atomic force microscope,” *Phys. Rev. Lett.*, Vol. 56, No. 9, pp. 930–933 (1986).
 13. Callister, W. D., *Materials Science and Engineering: an Introduction*. John Wiley and Sons, New York (1994).
 14. Case, J., L. Chilver, and C. T. F. Ross, *Strength of Materials and Structures*, 4th edition, John Wiley and Sons, New York (1999).
 15. Croft, D., G. Shed, and S. Devasia, “Creep, hysteresis, and vibration compensation for piezoactuators: atomic force microscopy application,” *ASME J. Dyn. Syst., Meas., Control*, Vol. 123, pp. 35–43 (2001).
 16. Schitter, G. and A. Stemmer, “Identification and open-loop tracking control of a piezoelectric tube scanner for high-speed scanning-probe microscopy,” *IEEE Trans. Control Syst. Technol.*, Vol. 12, No. 3, pp. 449–454 (2004).
 17. Li, Y. and J. Bechhoefer, “Feedforward control of a closed-loop piezoelectric translation stage for atomic force microscope,” *Rev. Sci. Instrum.*, Vol. 78, pp. 013702 (2007).
 18. Singhose, W. E., A. K. Banerjee, and W. P. Seering, “Slewing flexible spacecraft with deflection-limiting input shaping,” *AIAA J. Guid., Control, Dyn.*, Vol. 20, No. 2, pp. 291–298 (1997).
 19. Fleming, A. J. and A. G. Wills, “Optimal input signals for bandlimited scanning systems,” *Proc. IFAC World Cong.*, Seoul, Korea, July 7–11, pp. 11805–11810 (2008).
 20. Leang, K. K. and S. Devasia, “Feedback-linearized inverse feedforward for creep, hysteresis, and vibration compensation in AFM piezoactuators,” *IEEE Trans. Control Syst. Technol.*, Vol. 15, No. 5, pp. 927–935 (2007).
 21. Fleming, A. J. and K. K. Leang, “Evaluation of charge drives for scanning probe microscope positioning stages,” *Ultramicroscopy*, Vol. 108, No. 12, pp. 1551–1557 (2008).



Kam K. Leang received the B.S. and M.S. degrees in Mechanical Engineering from the University of Utah, Salt Lake City, Utah, in 1997 and 1999, respectively, and the Ph.D. degree from the University of Washington, Seattle, Washington, in 2004. He is an Assistant Professor in the Mechanical Engineering Department at the University of Nevada-Reno, Reno, Nevada, where he joined in 2008. From 2005 to 2008, he taught in the Mechanical Engineering Department at Virginia Commonwealth University, Richmond, Virginia. His research interests include modeling and control of piezoactuators for scanning probe microscopy applications, fabrication and control of electroactive polymers, and design of microelectromechanical systems (MEMS) for nanotechnology. He is a member of ASME, IEEE, and SPIE.



Andrew J. Fleming (M'03) was born in Dingwall, Scotland, in 1977. He received the B.S. degree in electrical engineering and the Ph.D. degree from The University of Newcastle, Callaghan, Australia, in 2000 and 2004, respectively. He is presently an Australian Research Council APD Fellow stationed at the School of Electrical Engineering and Computer Science, The University of Newcastle. In 2005, he was a Research Academic at the ARC Centre for Complex Dynamic Systems and Control, The University of Newcastle. His research includes microcantilever sensors, nanopositioning, and sensorless control of sound and vibration.